

Supporting Information

Neelin et al. 10.1073/pnas.1615333114

SI Text

Background on the First-Passage Process Simple Prototype. The simple stochastic prototype, Eq. 4, is used to approximate the moisture equation from the climate model, using the running accumulation \tilde{s} as a transformed temporal coordinate because it increases monotonically in time during a precipitation event but tracks an important physical variable, the integrated water loss due to precipitation. The steps implying the form of the accumulation distribution discussed in the text are expanded here. Once the problem is cast in the form of Eq. 4, and the noise term W is assumed to be from a Wiener process (Case 1 of the stochastic prototype), the corresponding Fokker–Planck equation has a classic form (29), except that \tilde{s} holds the place normally occupied by time. The evolution of the probability density $p_q = (q, \tilde{s})$ as a function of column-integrated moisture q and \tilde{s} is given by this equation, Eq. 6, repeated here for convenience:

$$\partial_{\tilde{s}} p_q(q, \tilde{s}) = \partial_q p(q, \tilde{s}) + \frac{1}{2} D \partial_q^2 p(q, \tilde{s}). \quad [\text{S1}]$$

For the first-passage problem, we consider that the precipitation event begins when the system first passes a threshold water vapor value q_0 and terminates when the water vapor drops below a slightly lower value $q_t = q_0 - \epsilon$, the threshold for precipitation termination. These conditions mimic the observed onset of precipitation at a critical value of column water vapor (for a given temperature profile), associated with conditional instability of entraining plumes or large-scale saturation in observations (22–24) and in versions of the climate model considered here (26, 27). Within this simple prototype, the onset corresponds to an initial condition of a delta function of probability density at q_0 , and the termination corresponds to an absorbing boundary condition with probability density $p_q = 0$ at q_t . The evolution of the pdf for this case has a known solution (28, 29)

$$p_q(q, \tilde{s}) = \frac{A_q}{\sigma(\tilde{s})} \left[F \left(\frac{q - q_0 + \tilde{s}}{\sigma(\tilde{s})} \right) - B F \left(\frac{q - q_0 + 2\epsilon + \tilde{s}}{\sigma(\tilde{s})} \right) \right], \quad [\text{S2}]$$

where $\sigma = (D\tilde{s})^{1/2}$, A_q is a normalization constant, and $B = \exp(2\epsilon/D)$ is set by the boundary condition $p_q = 0$ at the termination threshold. Note that the form $F(\cdot)$ is as in the scaling solution (Eq. 8), with the second occurrence shifted to maintain the boundary condition. For this case, F is simply a Gaussian. As the solution evolves forward in \tilde{s} , the probability of remaining above the termination threshold decreases by the mechanisms discussed in the main text. Evaluating the flux of probability across the termination threshold yields the probability that an event will terminate in a small increment surrounding a given \tilde{s} . This termination value of \tilde{s} defines the size s of the accumulation.

This yields an inverse Gaussian distribution for the accumulation pdf

$$p_s(s) = A_0 \exp[-sS/s] s^{-\tau} \exp[-s/s_L], \quad [\text{S3}]$$

where A_0 is a normalization constant, $\tau = 3/2$, and $s_L = 2D$ is the large-event cutoff, the key role of which is discussed in the main text. In the prototype full solution, there is also a small event cutoff $s_S = \epsilon^2/(2D)$, which Doppler radar measurements suggest may be on the order of 10^{-3} to 10^{-2} mm (18). In gauge observations (19, 20) and in the climate model analyzed here, the small event portion of the range is not resolved. Thus, the

distribution is simply considered over the range greater than the specified minimum accumulation $s_1 \gg s_S$, leading to the form

$$p_s(s) = A s^{-\tau} \exp[-s/s_L], \quad s > s_1 \quad [\text{S4}]$$

which corresponds to Eq. 7. The normalization constant A tends to be set by the smallest observable scale s_1 , because for $\tau > 1$, the low- s range dominates the integral when the power law range is long ($s_1 \ll s_L$). As a result, increases in large-event probability density due to increases in s_L create only a small adjustment in normalization constant, yielding small reductions in probability density over the power-law range. For instance, for $s_1 = 0.2$ mm, a change in s_L from 145 to 210 mm, as in the top curve of Fig. 1, yields only a 1% decrease in the normalization constant.

Note that the time-mean rainfall is not closely related to the changes in the accumulation distribution. The time mean obeys long-term constraints from moisture and energy budgets that can affect the fraction of time spent precipitating. The dry-spell intervals between precipitation events have dynamics with strong parallels to that considered here for accumulation distributions, with the upward drift in moisture toward onset of precipitation driven by mean moisture convergence, including evaporation. For increasing moisture convergence variance, the probability density of the very longest dry spells in the prototype tends to increase consistently with the results shown here for the change in pdf of the largest precipitation accumulations.

Considerations of Robustness and Relations with Other Systems.

Despite the complexity of the climate model, the simple stochastic prototype was able to provide predictions of its behavior. While the analytic solution for Case 1 and the scaling solution aim at distilling physical insight, the numerical solutions for Case 2 of the stochastic prototype make clear that the slight adjustments to the exponent of the power law range seen in the climate model solutions are easily obtained for assumptions that are realistic in a climate-modeling context. Here, we elaborate briefly on how the form of the regime change at a cutoff scale is robust to these changes. The Case 2 model is solved in the time domain, as for a climate model (note that D_* thus has different units than D). In Case 2, during nonprecipitating intervals, there is an upward drift in q due to \bar{C} . Event onset is taken to begin for precipitation above a small threshold, such that $P > \bar{C}$, and the drift is downward due to precipitation loss. The running accumulation \tilde{s} is then diagnosed within precipitation events in the Case 2 simulations. In this \tilde{s} coordinate, the Case 2 noise has temporal correlation and the spread of an ensemble of trajectories due to variations in moisture convergence increases less quickly than $\tilde{s}^{1/2}$, consistent with the slower drop of probability density of accumulation size at termination of the event in the approximately scale-free range before the cutoff. This behavior corresponds to the subdiffusive case of anomalous diffusion, as commonly arises in tracer transport in complex flow (41). Because the time dependence of the spreading process is different from that of the drift process, as seen in the scaling solution, a regime change with a cutoff scale given by the competition of these processes must occur. The amplitude of the moisture convergence variations is the key parameter in this competition—an increase in this amplitude with increasing moisture necessarily extends the cutoff, and thus creates the selective increase in probability density of the largest events. The physics of this competition must occur even for more complex moisture convergence variations, as in the climate model.

Prototypes for anomalous diffusion regimes and associated first-passage problems have been examined in a number of systems (42), so it is worth considering under what circumstances analogies drawn from these cases can be instructive. First-passage problem solutions exist for representation of these cases by fractional Fokker–Planck equations (43–45). A key result is that the properties discussed in the Weiner process case are modified smoothly, with the exponent of the power law range adjusted. Properties are in some cases approximated by a generalized inverse Gaussian distribution as in Eq. 3 where τ can differ from 3/2 (46), similar to features noted numerically in both Case 2 and CESM1 here. Technical challenges involving divergent moments often arise in these representations, including failure of the method of images under non-Markovian conditions (42, 47). The system of interest here is Markovian with finite moments, and thus in a number of respects is simpler than these cases. The adjustment of the exponent is here associated with the observable of climate interest—the time-integrated loss term.

Moment Ratio s_M and Large-Event Cutoff Geographic Dependence in the Climate Model. In the main text, an event-size scale s_M based on the ratio of second moment $\langle s^2 \rangle$ to the first moment $\langle s \rangle$ is used as an estimator proportional to the cutoff, as has been done to compare accumulation distributions for different regions estimated from the Department of Energy Atmospheric Measurement Program high-resolution observation sites (19)

$$s_M = \langle s^2 \rangle / \langle s \rangle. \quad [\text{S5}]$$

For the simple case (Eq. 3), the large-event cutoff s_L is related to s_M by

$$s_L = 2(\langle s^2 \rangle - \langle s \rangle^2) / \langle s \rangle \approx 2s_M. \quad [\text{S6}]$$

For Eq. 4, adjustments to the proportionality constant occur associated with s_1 and modifications to τ . A similar scaling also holds when the form of the cutoff $\exp[-s/s_L]$ is replaced by a

more general function $G[s/s_L]$ that approaches 1 for $s \ll s_L$ and 0 for $s \gg s_L$ (19, 20, 48). The form of a scale-free range followed by a cutoff is common to many systems. There is an underlying mathematical connection to the self-organized criticality literature that originally motivated observational work (18, 19)—certain first-passage processes can be put into one-to-one correspondence with simple models of self-organized criticality (29). Here, the derivation of the theoretical model from the equations of a climate model is key because we care foremost about the physical climate processes setting the cutoff in current climate and modifying it in future climate.

Fig. S1 shows the estimate of the large-event cutoff s_M in Eq. 6 as a spatial distribution for historical and end-of-century simulations, respectively. Fig. 3 shows the ratio of these. The full ensemble of 450 y is used, computing each of $\langle s \rangle$ and $\langle s^2 \rangle$ in Eq. 6. This first computation of such an estimate as a map shows spatial variations of s_M are considerable within current climate (Fig. S1a), with values increasing substantially toward the tropics. In many regions, a tendency may be noted for s_M to be larger over ocean regions than over land regions at comparable latitudes, likely associated with such factors as additional energy supply from the ocean surface and reduced impact of diurnal cycle. In the end-of-century case (Fig. S1b), large-scale spatial patterns remain similar, and the global warming increase in many areas can be seen primarily as a broad-scale increase on the order of 20%, albeit slightly larger in some regions than others, as seen in the ratio in Fig. 3. This serves as a reminder that the changes in probability density of the largest events seen in Figs. 1 and 2 are increases in the largest events experienced for a given geographic region. Large-event changes should not be misconstrued as converting midlatitude accumulation cutoffs to values typical of the tropics. Nonetheless, because the s_M changes translate into large changes in the pdf in the range of the very largest accumulations historically experienced in each region, these effects may be expected to play a key role for regional planners with regard to adaptation to potential flood magnitudes and other societal impacts.

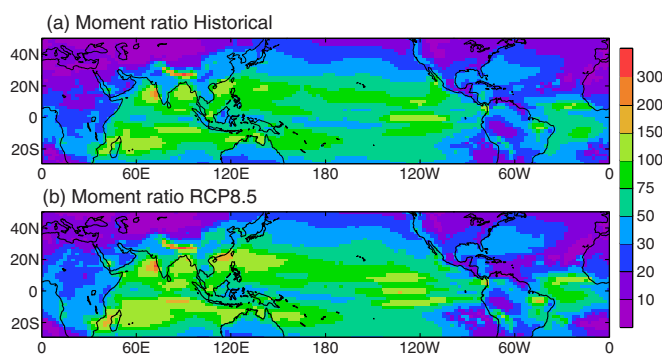


Fig. S1. The accumulation moment ratio, s_M (mm), an estimator proportional to the large-event cutoff value s_L . (A) For historical climate simulations (1976–2005). (B) For the end-of-century (2071–2100) simulations.

